Accuracy of quantitative reconstructions in SPECT/CT imaging

S Shcherbinin[1], A Celler[1], T Belhocine[2], R Vanderwerf[2] and A Driedger[2]

[1] Department of Radiology, University of British Columbia, 366-828 West 10th Avenue, Vancouver BC, V5Z 1L8, Canada
[2] Department of Nuclear Medicine, London Health Sciences Centre, 375 South Street, PO Box 5375, London ON, N6A 4G5, Canada

E-mail: shcher2@interchange.ubc.ca

Abstract

The goal of this study was to determine the quantitative accuracy of our OSEM-APDI reconstruction method based on SPECT/CT imaging for Tc-99m, In-111, I-123, and I-131 isotopes. Phantom studies were performed on a SPECT/low-dose multislice CT system (Infinia-Hawkeye-4 slice, GE Healthcare) using clinical acquisition protocols. Two radioactive sources were centrally and peripherally placed inside an anthropometric Thorax phantom filled with non-radioactive water. Corrections for attenuation, scatter, collimator blurring and collimator septal penetration were applied and their contribution to the overall accuracy of the reconstruction was evaluated. Reconstruction with the most comprehensive set of corrections resulted in activity estimation with error levels of 3–5% for all the isotopes.

(Some figures in this article are in colour only in the electronic version)

1. Introduction

Accurate quantitation of activity distribution is one of the key elements for unsealed radiotherapy procedures (Flux *et al* 2006). With increased availability of hybrid imaging, simultaneous assessment of organ anatomy and function has become clinically both feasible and practical. More importantly, such dual-modality imaging allows for advanced data processing, which may potentially lead to fully quantitative measurement of radiotracer distribution in tumors, more accurate than is possible with other currently available methods.

The main limitation of SPECT/CT in providing quantitative information about the activity distribution is related to the severe degradation of the acquired data by different physics effects (Tsui *et al* 1998, El Fakhri *et al* 2000, King *et al* 2004, Buvat 2007). These image-degrading factors include attenuation and scattering of photons as they pass through different layers of

tissue, and resolution loss due to collimator blurring. The relative impact of these phenomena on the SPECT quantitative accuracy was investigated, for instance, by El Fakhri *et al* (2000), Buvat *et al* (2000) and He *et al* (2005).

Incorporation of an accurate description of physics phenomena into reconstruction algorithms serves as an effective way to improve quantitative characteristics of the recovered image. In hybrid SPECT/CT imaging systems, the spatial distribution of attenuation coefficients is obtained from CT scans (e.g., Hasegawa *et al* (2002) and Hasegawa and Zaidi (2006)). The collimator blurring can be described by a 3D Gaussian function. However, accurate modeling of photons scattered through non-uniform media still represents a challenging task (Zaidi and Koral 2006) even when using patient-specific CT-based attenuation maps. Because the behavior of scattered photons depends on electron density in every point of the scanned object, its calculation is very expensive in terms of computation time. Both Monte Carlo simulations (Veklerov *et al* 1988, Floyd *et al* 1989, Bowsher and Floyd 1991, Lazaro *et al* 2005) and analytical integration of the Klein–Nishina formula (Cao *et al* 1994, Riauka and Gortel 1994, Wells *et al* 1998) are affected by this factor.

Our analytical photon distribution (APD) method (Wells *et al* 1998) of scatter modeling uses the later approach where noiseless scatter projections are analytically calculated using the Klein–Nishina formula. Our method utilizes 3D CT-based attenuation maps to estimate attenuation and scatter of propagating photons without any simplifications regarding homogeneousness of patient tissues or physics of photons propagation through non-uniform media (see the list of assumptions below). Neither 'effective scatter source estimations' (ESSE) (Frey and Tsui 1996) nor 'effective scatter source images' (ESSI) (Bai *et al* 2000) are employed.

The techniques used to shorten the computation time for our quantitative image reconstruction (which includes attenuation, scatter and resolution recovery corrections) are as follows.

- Only first- and second-order Compton as well as Rayleigh scatter components are directly calculated using the Klein–Nishina formula. If necessary, to correct for photons that scattered more than twice, the scaling factor matching experimental and APD-computed projections may be introduced (Vandervoort *et al* 2005).
- A substantial part of the calculations can be performed just once and saved as camera-dependent look-up tables to be used in any later acquired patient study (Wells *et al* 1998). Fast calculation of these look-up tables is performed using the advanced numerical integration techniques (Humphries *et al* 2007).
- Additionally, a substantial improvement in calculation time and computer memory requirements is achieved by using interpolated scatter point spread functions—APD-interpolated (APDI) method (Vandervoort *et al* 2005).
- While attenuation and resolution recovery corrections are incorporated directly into the system matrix, the scatter component is included only in the forward step of the MLEM/OSEM algorithm.

Experimental validation of this technique performed previously using Tc-99m and cardiac phantom data demonstrated errors of quantitative estimation of activity concentration below 4% (Vandervoort *et al* 2007).

A broad, long-term objective of our research is to create a practical methodology that would enable quantitative data acquisition and image reconstruction for clinical oncology applications, subsequently leading to accurate and patient specific dosimetry calculations for internal radiation therapy procedures. The goal of this particular study was to determine the quantitative accuracy of SPECT reconstructions that can be achieved in a clinical environment

Table 1. Parameters and results of sample quantitative SPECT studies with physical phantoms.

Study	Radiotracer	Camera	Results of absolute quantitation
He *et al* (2005)	In-111	GE Discovery VH/Hawkeye	2–12% errors for 6 and 20 ml spheres
de Wit *et al* (2006)	Ho-166	ADAC Vertex MCD	1–13% errors for 220 ml cylindrical containers
Du *et al* (2006)	I-123	Siemens E.cam	2% errors for regions of brain phantom
Koral *et al* (2007)	I-131	Prism 3000	1–24% errors for 7–135 ml spheres
Vandervoort *et al* (2007)	Tc-99m	Siemens E.cam	4% errors for 18 ml heart chamber

for four different radioisotopes (Tc-99m, I-123, I-131 and In-111) commonly used in oncology when utilizing consistent acquisition and reconstruction protocols. In particular, ^{99m}Tc-MDP bone scan, $^{131/123}$I-MIBG and ^{111}In-Octreoscan in oncological indications (i.e. detection of bone metastases, neuroendocrine tumors) were considered. Some of these isotopes (I-123, I-131) emitting high-energy photons contribute to the so-called crosstalk effect when these energetic photons scatter and get recorded in the imaging energy window, and increase background due to collimator septal penetration. So, the algorithm previously developed for Tc-99m (Vandervoort *et al* 2005, 2007) needed to be modified to meet these new requirements.

Several recent studies were devoted to the investigation of absolute quantitation of SPECT using physical phantoms (e.g., He *et al* (2005), de Wit *et al* (2006), Du *et al* (2006), Koral *et al* (2007) and Vandervoort *et al* (2007)). These studies, however, were performed using a variety of different cameras, different correction techniques and different methods for determination of an absolute activity (table 1).

In contrast, all our phantom experiments were performed using one and the same integrated SPECT/CT system, the Infinia-Hawkeye-4 SPECT/CT camera, with identical acquisition matrices and camera rotations. One and the same reconstruction OSEM-APDI scheme (Vandervoort *et al* 2005) with attenuation (AC), scatter (SC) and resolution recovery (RR) corrections was applied. For both iodine isotopes (I-123 and I-131) emitting high-energy (>500 keV) photons, an identical approach was used to correct the data for crosstalk and collimator septal penetration.

In our measurements of absolute activity, we did not assume that the shape of the investigated object is known, as in clinical situations the boundaries between tumors and healthy tissues often are not well defined and cannot be easily estimated from the CT scans. Instead, we applied two different thresholds to reconstructed images: one to determine the total activity in the object (tumor) and the second to estimate the volume (number of voxels) occupied by the object, and compared the resulting values of the activity and volume with the true ones.

2. Methods

2.1. Experiments

Our experimental setup was designed to model clinical SPECT/CT studies for oncological indications. Accordingly, two identical cylindrical bottles (diameter 26 mm, height 60 mm, volume 32 ml each), containing investigated activity, played the role of tumors. These two radioactive sources were placed at different depths (one central source and one peripheral source) in the thorax phantom (Data Spectrum Corp.), which in our experiments was filled with cold (non-radioactive) water. Experiments were set up with Tc-99m, I-123, I-131 and In-111 isotopes to simulate different clinical studies such as ^{99m}Tc-MDP bone scan for detection

Table 2. Parameters of acquisition experiments.

Radiotracer	Tc-99m	I-123	I-131	In-111
Detector	LEHR	LEHR	HEGP	MEGP
Number of frames	90	90	90	90
Number of camera stops	45	45	45	45
Angular step (grad)	4	4	4	4
Acquisition time per frame (s)	30	30	30	30
Lower energy window (keV)	126.0–154.0	143.1–174.9	327.6–400.4	153.9–188.1 220.5–269.5
Upper energy window (keV)	–	180.0–220.0	405.0–495.0	–
Matrix dimension	128	128	128	128
Pixel size, mm	4.42	4.42	4.42	4.42
Activity in bottle 1 (MBq)	10.24	3.64	13.89	13.98
Activity in bottle 2 (MBq)	10.24	3.60	13.99	13.59
Number of counts per projection detected in lower window	14 300	7500	14 300	28 700
Number of counts per projection detected in upper window	–	4600	5800	–

of bone metastases, and ^{123}I-MIBG, ^{131}I-MIBG and ^{111}In-Octreoscan for evaluation of neuroendocrine tumors. Our experimental configuration was intended to replicate oncological studies which are characterized by high tumor uptake with very low or practically no activity in the background.

The experimental data were acquired on the Infinia-Hawkeye-4 (GE Healthcare), an integrated SPECT/low-dose multislice CT system (2.5 mA; 140 kVp), using conventional clinical protocols. For each isotope, the energy windows were set according to clinical protocols used for ^{99m}Tc-MDP bone scan, $^{131/123}$I-MIBG and ^{111}In-Octreoscan. For I-123 and I-131 data, a second energy window was established to measure intensity of high-energy photons, to be used in crosstalk and collimator septal penetration correction (SPC). Detailed information about our experimental setup is presented in table 2. The locations of bottles inside the phantom are shown in figure 1.

To translate the measured counts into the absolute values of reconstructed activities, we performed calibration experiments. For each isotope, a planar 5 min scan was performed using a point source (calibrated using the well counter) and placed in air at a distance of about 20 cm from the detector surface. The acquisition matrices and energy windows were exactly the same as for the corresponding phantom studies.

2.2. Reconstruction algorithms

From these experimental data, we reconstructed a series of 3D images using the ordered subsets expectation maximization method (OSEM) with 4-12 iterations and 5-10 subsets including different sets of corrections. The system of algebraic equations,

$$CX = Y, \tag{1}$$

modeling the SPECT acquisition process, was solved using the following iterative formula:

$$X_j^{(n+1)} = \frac{X_j^{(n)}}{\sum_{i \in \Omega} C_{ij}} \sum_{i \in \Omega} C_{ij} \frac{Y_i}{\sum_k C_{ik} X_k^{(n)} + F_i} \tag{2}$$

where X corresponds to the unknown vector of activity distribution; Y is the vector corresponding to the measured projection data; C_{lm} is the system matrix element representing
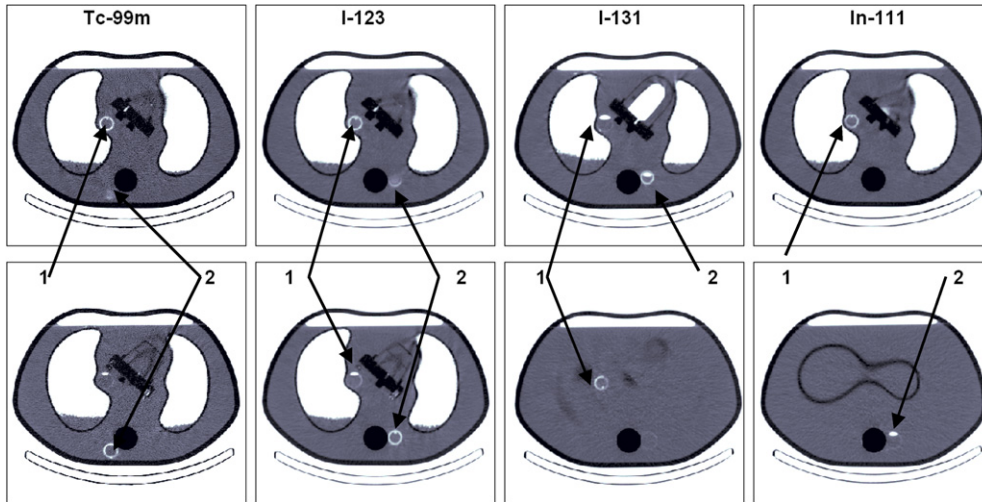
Figure 1. Sample CT slices from the SPECT/CT experiments with Tc-99m, I-123, I-131 and In-111, respectively. The arrows show the locations of bottle 1 and bottle 2. As due to their locations, both bottles often could not be seen in the same slice, two different slices are displayed.

the probability that the photon emitted from the mth voxel is detected in the lth pixel; n denotes the iterations' counter; and F is the vector used to incorporate scatter, crosstalk and septal penetration corrections into the reconstruction process (see below).

The RR was implemented in all our reconstructions directly into the system matrix (Blinder *et al* 2001). The camera response was modeled by 3D Gaussian functions with the depth-dependent full width at half maximum (FWHM) empirically determined for each (LEHR, MEGP and HEGP) collimator.

SPC was included in all reconstructions for I-123 and I-131 data. This correction was performed using the projection data acquired in the upper energy window (e.g., Koral *et al* (2007)). Specifically, we calculated the contribution H_{LW} of high-energy photons as

$$H_{LW} = K\{H_{UW}\} \tag{3}$$

where H_{UW} is the distribution of photons recorded within the upper energy window (UW), $\{*\}$ designates the Wiener smoothing operation applied to each 2D projection and K is the scaling coefficient estimated by comparing the same background regions in LW and UW projections. The estimated distribution H_{LW} was incorporated into F in the forward step in formula (2).

In terms of attenuation and scatter corrections, we considered the following hierarchy of reconstructions.

 (i) Neither attenuation nor scatter corrections were applied.
 (ii) Attenuation correction was done using CT-based attenuation maps. Further, in order to additionally account for scatter correction, this map was scaled to broad-beam (BB) attenuation coefficient values (by multiplying all map voxels by a factor of 0.8) and incorporated into the system matrix C. This approach (BB-attenuation correction) is supposed to approximately take contribution from the scattered photons into account (Jaszczak *et al* 1981). For In-111, since only one data set was acquired for both energy windows, the attenuation map was rescaled to an 'effective' energy (based on the energy spectrum available from Monte Carlo simulations (Assie *et al* 2005)).

(iii) The CT-based attenuation map was normalized to narrow-beam (NB) attenuation coefficients (therefore, attenuation correction did not account for scattered photons) and incorporated into the system matrix C. The distribution of scattered photons was accurately computed using the analytical APDI method (Wells *et al* 1998, Vandervoort *et al* 2005) from the initial activity reconstruction and the CT-based attenuation map, and incorporated into the F component in formula (2) (Vandervoort *et al* 2005). In summary, AC and RR were implemented directly into the system matrix C, and scatter and septal penetration components were estimated separately using the above-described methods and incorporated (as vector F) only into the forward step of OSEM. Accordingly, the correction vector F in formula (2) contains scatter components for Tc-99m and In-111, and both scatter and high-energy components for I-123 and I-131 cases.

In all reconstructions, 5-10 subsets and 4-12 OSEM iterations were used. In case (iii), we performed four OSEM iterations with the BB map and no scatter correction. Then, we used APDI and the NB map to calculate the scatter component; additionally, we conducted further eight iterations with scatter correction included in the vector F. When a CT-based attenuation map is used, such a single update of the scatter component leads to more quantitatively accurate results than achieved with multiple scatter updates.

2.3. Data analysis

In order to perform a quantitative analysis of our reconstructions, we applied two 3D thresholds to each image. The thresholds were based on the average over eight voxels maximum in each investigated region (corresponding to the bottle location). The total activity A in the container was measured by integrating all counts inside the volume of interest (VOI) determined by the threshold set at 1% level. In this VOI-1%, basically all the counts originating from a given object are included. The measured total volume V of each object was estimated as a number of voxels with counts equal to or larger than 20.0% of the averaged maximum. According to our preliminary tests, the VOI-20% allows us for relatively better determination of volumes than can be done using other thresholds.

3. Results

In tables 3 and 4, the results for quantification of activities (ΔA, %) and volumes (ΔV, %) are detailed for the 1% threshold (VOI-1%) and the 20% threshold (VOI-20%), respectively. In both tables, the relative differences between the true and measured activities ($\Delta A = $ ('true' $A - $ 'measured' A)/'true' A) and between true and estimated volumes of bottles ($\Delta V = $ ('true' $V - $ 'measured' V)/'true' V) are displayed. The 'true' V was determined as a number of voxels corresponding to the volume (32 ml) of sources. We also visually confronted the calculated areas of sources and corresponding fragments of CT scans. The first row in these two tables corresponds to the reconstructions with RR and SPC (for I-123 and I-131 isotopes), but without either AC or SC. The second row presents the results of reconstructions with a CT-based attenuation map scaled to the BB values. The third row of each table summarizes the results obtained using our most sophisticated procedure which employs RR, CSP, NB-based AC and APDI-based SC.

The results presented in table 3 clearly indicate that the highest accuracy of activity determination was achieved for OSEM-APDI reconstructions which included corrections for all image-degrading factors. For all Tc-99m, In-111, I-131 and I-123 isotopes, the relative errors between the 'true activities' and the reconstructed 'measured activities' were about 5% of the total activity values as determined by the VOI-1% (row 3, table 3). However, the

Table 3. Comparison of quantitative accuracy of different reconstruction schemes. The relative differences between the true and calculated activities (ΔA, %) and volumes (ΔV, %) as obtained with VOI-1% for the central (1) and the peripheral (2) sources are presented.

AC	SC	Vial	Tc-99m 1	Tc-99m 2	I-123 1	I-123 2	I-131 1	I-131 2	In-111 1	In-111 2
–	–	ΔA, %	−84.3	−71.2	−81.8	−75.0	−73.7	−69.3	−80.7	−74.8
		ΔV, %	216	261	325	460	537	556	375	530
BB	–	ΔA, %	−21.4	1.3	−17.9	0.3	−16.6	−6.7	−18.4	−1.3
		ΔV, %	287	328	302	386	469	512	401	494
NB	APDI	ΔA, %	−2.9	3.6	−4.1	5.1	−4.0	3.3	−4.5	3.5
		ΔV, %	152	135	140	156	325	434	207	206

Table 4. Comparison of quantitative accuracy of different reconstruction schemes. The relative differences between the true and calculated activities (ΔA, %) and volumes (ΔV, %) as obtained with VOI-20% for the central (1) and the peripheral (2) sources are presented.

AC	SC	Vial	Tc-99m 1	Tc-99m 2	I-123 1	I-123 2	I-131 1	I-131 2	In-111 1	In-111 2
–	–	ΔA, %	−89.8	−76.7	−87.4	−81.8	−84.0	−79.4	−86.4	−81.2
		ΔV, %	−34	7	−18	0	−9	6	−4	21
BB	–	ΔA, %	−41.1	−19.2	−39.8	−25.4	−46.7	−36.5	−42.0	−26.7
		ΔV, %	−9	9	−9	1	−4	7	−1	18
NB	APDI	ΔA, %	−18.6	−10.8	−19.9	−12.0	−31.4	−25.7	−24.1	−16.9
		ΔV, %	−7	−1	−9	−7	−6	0	−5	−1

volumes of sources were overestimated by a factor of 2.5–5.5 when the same threshold was used for volume determination. As expected, the total reconstructed activity was significantly underestimated in images reconstructed without attenuation correction, (row 1, table 3). When attenuation correction but no accurate scatter correction is applied (BB attenuation map), the errors strongly depend on the location of the sources: one could almost accidentally achieve low or high accuracy levels. In our experiments these errors ranged from 0.3% to 21.4% (row 2, table 3).

For all considered cases, the threshold of 20% allowed us to estimate the volume of the source with errors lower than 9% (row 3, table 4). Even after applying all the corrections, this threshold does not provide an accurate activity estimate and the total activity inside VOI-20% differed from the true values by 11–31%. The dependences of the accuracy of quantification (ΔA and ΔV) on the values of thresholds for Tc-99m, I-123, I-131 and In-111 are detailed in figure 2.

4. Discussion

For both SPECT and PET techniques, the accurate measurement of tracer distribution into normal and abnormal structures is critical for diagnostic and treatment purposes (Thierens *et al* 2005).

In clinically realistic situations, when the volume of the source cannot be precisely determined, the definition of 'quantitation' might mean two different things: the accurate estimation of total activity and the volume of the source. In our phantom study, we used an
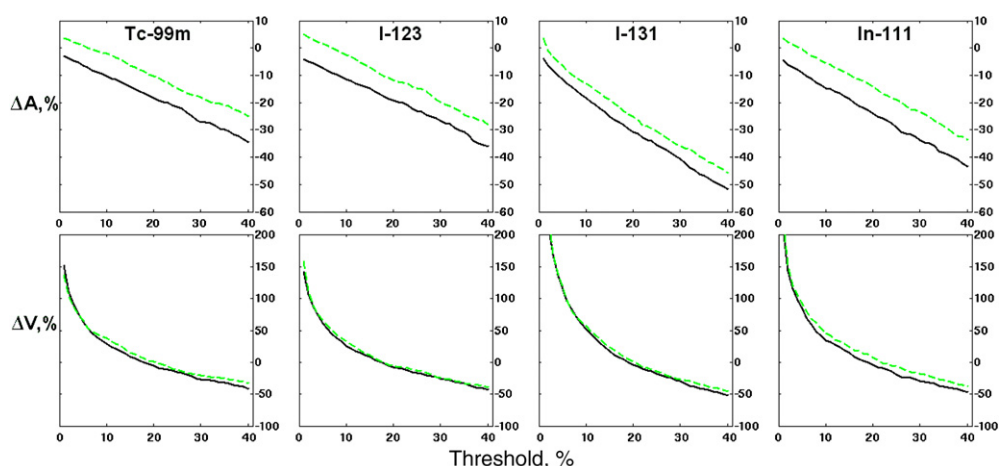
Figure 2. Dependence of ΔA (upper row) and ΔV (lower row) on the threshold (%) for OSEM-APDI reconstructions. The solid line corresponds to source 1 and the dashed line to source 2.

integrated SPECT/CT system allowing a high-quality CT-based AC together with SC, RR and SPC. In addition, the CT unit of our hybrid camera was useful for anatomic localization of Tc-99m, I-123, I-131 and In-111 sources located centrally and peripherally to simulate mediastinal and spinal metastases, respectively.

Our results demonstrate that these two characteristics, namely activity and volume, cannot be reliably determined when using the same threshold. We found, however, that the images obtained from our OSEM-APDI reconstruction method, which includes corrections for most of the physical processes, become relatively independent of the characteristics of the isotope and the detection system. This feature allowed us to use a consistent set of thresholds to determine the total activities and volumes for both investigated objects and for all isotopes. We achieved the errors about 5% for determination of the total activity at the 1% threshold, and <9% errors for determination of the volume at 20% threshold for all isotopes in centrally and peripherally located sources.

However, these results are based on four experiments with only eight identical 32 ml active sources placed inside inactive background. The absence of spill-in effect from background and usage of sources of identical size and shape allowed us to use simple and identical quantification techniques for all active containers. Quantification of smaller (with size less than ∼3*FWHM) sources may require different thresholds (King *et al* 1991). The presence of background activity and spill-in effect will require more sophisticated procedures, for example, adaptive thresholds including an uptake/background ratio. As was mentioned above, we compared the 'true' and 'measured' volumes as total number of voxels without explicitly detecting edges of sources which are assumed to be unknown. The determination of the 'true' volume as number of voxels located inside known boundaries may change the calculated values of ΔV.

As seen in tables 3 and 4 (row 3), the reconstructed activities of the sources located peripherally (near the spine of the phantom) were 5–9% higher than those located in the center of the phantom. We explain these differences by the inaccuracies of the CT-based attenuation maps which may be critical when the source is located near the boundary between materials with different attenuation coefficients such as water and lung (source 1) or water and spine (source 2). To confirm that statement, we performed additional tests reconstructing

the digital data created by Monte Carlo simulations with Tc-99m activity. In these tests, our numerical phantom exactly modeled the experimental one. When the same attenuation map was used for data creation and reconstruction, the differences between activities reconstructed in the objects at different locations were only 0.1%, but slight misalignment of the attenuation map and the emission data by 1 voxel (4.4 mm) led to the difference of 5–7% between these activities. Such misalignment may be related to errors in rescaling the CT image matrix to that of the attenuation map or can occur when CT and NM cameras are not perfectly registered. Attenuation correction with quality control (ACQC) will be useful for correction of misalignment between CT (transmission) and NM (emission) data on integrated SPECT/CT systems (Chen *et al* 2006, Fricke *et al* 2004). In addition, in our phantom experiment, potential errors in rescaling the attenuation coefficients for the teflon (spine) should be taken into consideration. According to Watson *et al* (2006), such errors may occur when performing quantitative PET/CT analysis with phantoms containing several man-made materials.

5. Conclusions

Our OSEM-APDI reconstruction procedure for quantitative SPECT-CT imaging demonstrated an accurate determination of the absolute activity and volume for Tc-99m, I-123, I-131 and In-111. CT-based attenuation correction and resolution recovery were directly incorporated into the system matrix, while scatter and septal penetration components were separately calculated and incorporated into the forward step of the reconstruction process. From four phantom experiments with eight active sources of identical size and shape surrounded by inactive background, we recovered 95–105% of the true total activity by using a 1% threshold, and 91–100% of the true source volume by using a 20% threshold irrespective of the isotope/detector and source location. Further clinical simulations are needed to validate our encouraging results.

References

Assie K, Gardin I, Vera P and Buvat I 2005 Validation of the Monte Carlo simulator GATE for indium-111 imaging *Phys. Med. Biol.* **50** 3113–25

Bai C, Zeng G L and Gullberg G T 2000 A slice-by-slice blurring model and kernel evaluation using the Klein–Nishina formula for 3D scatter compensation in parallel and converging beam SPECT *Phys. Med. Biol.* **45** 1275–307

Blinder S, Celler A, Wells R G, Thompson D and Harrop R 2001 Experimental verification of 3D detector response compensation using the OSEM reconstruction method *IEEE Nucl. Sci. Symp. Rec.* pp 2174–8

Bowsher J E and Floyd C E Jr 1991 Treatment of Compton scattering in maximum-likelihood, expectation maximization reconstructions of SPECT images *J. Nucl. Med.* **32** 1285–91

Buvat I 2007 Quantification in emission tomography: challenges, solutions, and performance *Nucl. Instrum. Methods Phys. Res.* A **571** 10–3

Buvat I, Soret M, Hapdey S, Riddell C, Benali H and Di Paola R 2000 Respective importance of scatter, collimator response, and partial volume effect corrections for accurate quantification ^{123}I dopamine receptor imaging *IEEE Nucl. Sci Symp. Rec.* pp 13/15–13/19

Cao Z-J, Frey E C and Tsui B M W 1994 A scatter model for parallel and converging beam SPECT based on the Klein–Nishina formula *IEEE Trans. Nucl. Sci.* **41** 1594–600

Chen J, Caputlu-Wilson S F, Shi H, Galt J R, Faber T L and Garcia E V 2006 Automated quality control of emission-transmission misalignment for attenuation correction in myocardial perfusion imaging with SPECT-CT systems *J. Nucl. Cardiol.* **13** 43–9

de Wit T C, Xiao J, Nijsen J F W, van het Schip F D, Staelens S G, van Rijk P P and Beekman F J 2006 Hybrid scatter correction applied to quantitative holmium-166 SPECT *Phys. Med. Biol.* **51** 4773–87

Du Y, Tsui B M W and Frey E C 2006 Model-based compensation for quantitative ^{123}I brain SPECT Imaging *Phys. Med. Biol.* **51** 1269–82

El Fakhri G, Buvat I, Benali H, Todd-Pokropek A and Di Paola R 2000 Relative impact of scatter, collimator response, attenuation, and finite spatial resolution corrections in cardiac SPECT *J. Nucl. Med.* **41** 1400–8

Floyd C E, Jaszczak R J and Coleman R E 1989 InverseMonte Carlo: a unified reconstruction algorithm *IEEE Trans. Nucl. Sci.* **32** 779–85

Flux G, Bardies M, Monsieurs M, Savolainen S, Strand S-E and Lassmann M 2006 The impact of PET and SPECT on dosimetry for targeted radionuclide therapy *Z. Med. Phys.* **16** 47–59

Frey E C and Tsui B M W 1996 A new method for modelling the spatially-variant, object dependent scatter response function in SPECT *IEEE Nucl. Sci. Symp. Rec.* pp 1305–7

Fricke H, Fricke E, Weise R, Kammeier A, Lindner O and Burchert W 2004 A method to remove artifacts in attenuation-corrected myocardial perfusion SPECT Introduced by misalignment between emission scan and CT-derived attenuation maps *J. Nucl. Med.* **45** 1619–25

Gilland D R, Jaszczak R J, Turkington T G, Greer K L and Coleman R E 1994 Volume and activity quantitation with iodine-123 SPECT *J. Nucl. Med.* **35** 1707–13

Hasegawa B H, Wong K H, Iwata K, Barber W C, Hwang A B, Sakdinawat A E, Ramaswamy M, Price D C and Hawkins R A 2002 Dual-modality imaging of cancer with SPECT/CT *Technol. Cancer Res. Treat.* **1** 417–508

Hasegawa B H and Zaidi H 2006 Dual-Modality imaging: more than the sum of its components *Quantitative Analysis in Nuclear Medicine Imaging* ed H Zaidi (Berlin: Springer) pp 35–81

He B, Du Y, Song X, Segars W P and Frey E C 2005 A Monte Carlo and physical phantom evaluation of quantitative In-111 SPECT *Phys. Med. Biol.* **50** 4169–85

Humphries T, Celler A and Trummer M R 2007 Improved numerical integration for analytical photon distribution calculation in SPECT *IEEE Nucl. Sci. Symp. Rec.* pp 3548–54

Jaszczak R, Coleman R and Whitehead F 1981 Physical factors affecting quantitative measurements using camera-based single photon emission computed tomography (SPECT) *IEEE Trans. Nucl. Sci.* **NS-28** 69–79

King M A, Glick S J, Pretorius P H, Wells R G, Gifford H C, Narayanan M V and Farncombe T 2004 Attenuation, scatter, and spatial resolution compensation in SPECT *Emission Tomography. The Fundamentals of PET and SPECT* ed M N Wernick and J N Aarsvold (New York: Academic) pp 473–98

King M A, Long D T and Brill A B 1991 SPECT volume quantitation: influence of spatial resolution, source size and shape, and voxel size *Med. Phys.* **18** 1016–24

Koral K F, Yendiki A and Dewaraja Y K 2007 Recovery of total I-131 activity within focal volumes using SPECT and 3D OSEM *Phys. Med. Biol.* **52** 777–90

Lazaro D, El Bitar Z, Breton V, Hill D and Buvat I 2005 Fully 3D Monte Carlo reconstruction in SPECT: a feasibility study *Phys. Med. Biol.* **50** 3739–54

Riauka T and Gortel Z 1994 Photon propagation and detection in single-photon computed emission tomography—an analytical approach *Med. Phys.* **21** 1311–21

Thierens H M, Monsieurs M A and Bacher K 2005 Patient dosimetry in radionuclide therapy: the whys and the wherefores *Nucl. Med. Commun.* **26** 593–9

Tsui B M W, Frey E C, LaCroix K J, Lalush D S, McCartney W H, King M A and Gullberg G T 1998 Quantitative myocardial perfusion SPECT *J. Nucl. Cardiol.* **5** 507–22

Vandervoort E J, Celler A and Harrop R 2007 Implementation of an iterative scatter correction, the influence of attenuation map quality and their effect on absolute quantitation in SPECT *Phys. Med. Biol.* **52** 1527–45

Vandervoort E J, Celler A, Wells R G, Blinder S, Dixon K L and Pang Y 2005 Implementation of an analytically based scatter correction in SPECT reconstructions *IEEE Trans. Nucl. Sci.* **52** 645–53

Veklerov E, Llacer J and Hoffman E 1988 MLE reconstruction of a brain phantom using a Monte Carlo transition matrix and a statistical stopping rule *IEEE Trans. Nucl. Sci.* **35** 603–7

Watson C C, Rappoport V, Faul D, Townsend D W and Carney J P 2006 A method for calibrating the CT-based attenuation correction of PET in human tissues *IEEE Trans. Nucl. Sci.* **53** 102–7

Wells R G, Celler A and Harrop R 1998 Analytical calculation of photon distribution in SPECT projections *IEEE Trans. Nucl. Sci.* **45** 3202–14

Zaidi H and Koral K F 2006 Scatter correction strategies in emission tomography *Quantitative Analysis in Nuclear Medicine Imaging* ed H Zaidi (Berlin: Springer) pp 205–35

Zeng G L, Bai C and Gullberg G T 1999 A projector/backprojector with slice-to-slice blurring for efficient three-dimensional scatter modeling *IEEE Trans. Med. Imaging* **18** 722–32